Diffusion MRI Anisotropy in the Cerebral Cortex is Determined by Unmyelinated Tissue Features

Colin Reveley[1,2,*], Frank Q Ye[3], Rogier B Mars[1,4], Denis Matrov[5], Yogita Chudasama[5], David A Leopold[3,6]

[1] Wellcome Centre for Integrative Neuroimaging, Centre for fMRI of the Brain (FMRIB), Nuffield Department of Clinical Neurosciences, John Radcliffe Hospital, University of Oxford, Headington, Oxford, OX9 3DU, UK.

[2] Department of Informatics, University of Sussex, Falmer, Brighton BN1 9QJ, UK

[3] Neurophysiology Imaging Facility, National Institute of Mental Health, National Institute of Neurological Disorders and Stroke, National Eye Institute, National Institutes of Health, Bethesda, MD

[4] Donders Institute for Brain, Cognition and Behaviour, Radboud University Nijmegen, Nijmegen, The Netherlands.

[5] Section on Behavioral Neuroscience, National Institute of Mental Health, National Institutes of Health, Bethesda, MD

[6] Section on Cognitive Neurophysiology and Imaging, Laboratory of Neuropsychology, National Institute of Mental Health, National Institutes of Health, Bethesda, MD

*correspondence: reveley@gmail.com

Abstract

Diffusion magnetic resonance imaging (dMRI) is commonly used to assess the tissue and cellular substructure of the human brain. In the white matter, myelinated axons are the principal neural elements that shape dMRI through the restriction of water diffusion; however, in the gray matter the relative contributions of myelinated axons and other tissue features to dMRI are poorly understood. Here we investigate the determinants of diffusion in the cerebral cortex. Specifically, we ask whether myelinated axons significantly shape dMRI fractional anisotropy (dMRI-FA), a measure commonly used to characterize tissue properties in humans. We compared ultra-high resolution *ex vivo* dMRI data from the brain of a marmoset monkey with both myelin- and Nissl-stained histological sections obtained from the same brain after scanning. We found that cortical diffusion was only minimally related to the density and arrangement of myelinated fibers. Instead, the spatial pattern of dMRI-FA in the cortex was more closely related to anisotropy of tissue features indicated in the Nissl stained sections. Our results suggest that unmyelinated neurites such as large caliber apical dendrites are the primary features shaping dMRI measures in the cerebral cortex.

Introduction

Recent advances in high resolution diffusion MRI (dMRI) methods have revealed significant diffusion anisotropy in the cerebral cortex gray matter[1–8]. This finding provides an opportunity to extend the use of dMRI beyond its well-established application for characterizing white matter projections. Determining the cellular and histological features that give rise to this anisotropy is important, because it could offer a way for MRI methods to detect and measure the detailed cytoarchitectural properties of gray matter, both in healthy tissue and in disease states. Cytoarchitecturally grounded MRI contrasts could aid in the detection of neuropathology by linking foundational histological studies in the medical field[9] to *in vivo* studies in humans at the level of individual subjects. For example, linking dMRI variation to tissue structure could be applied to track the progression of cortical pathology during the early stages of Alzheimer's disease[10], or to track tissue changes in conditions like PTSD[11].

The histological basis of diffusion anisotropy in gray matter is not yet well explored[12]. Based on principles derived from the analysis of white matter, where the majority of previous histological comparisons have been carried out[13,14], one possibility is that cortical dMRI patterns most directly reflect the density and arrangement of myelinated fibers[2,8,15–21]. Large caliber axons, similar to those in white matter, can also be found in gray matter. For example some large incoming and outgoing axonal projections run vertically through the cortex into the underlying white matter [8,22,23]. However, these are relatively sparse, and are only one aspect of gray matter myeloarchitecture. Myelinated axons in the gray matter are often organized very differently than in the white matter, with less dense packing, smaller caliber fibers, and sometimes a matted, rather than bundled, mesoscopic structure[24].

The spatial distribution of cortical myelin density varies substantially by horizontal location (anatomical region) and by vertical (laminar) position. The myelin content of voxels may be assessed using a wide variety of MRI contrasts[13,14,25], such as the T1w/T2w or magnetization transfer ratio (MTR). In fact, myelin density is currently the principal means by which MRI is used to estimate the histological boundaries of cortical areas in the human brain in-vivo[26]. Quantitative assessment of MRI sensitivity to myelin, including the potential role of diffusion MRI (dMRI), is a topic of active research[13,14,25]. For dMRI specifically, some evidence suggests that the cortical variation of fractional anisotropy is determined more directly by the organizational structure of myelinated fibers, rather than by their density *per se*[3,27], although this prospect has not yet been demonstrated quantitatively[2]. Histological analysis of the cortex

80 has revealed significant variation in the organization of myelinated axons from region to region,[24,28] to
81 which diffusion anisotropy may be sensitive.

82 However, compared to white matter, myelinated axons are a comparatively small component of
83 gray matter tissue structure. The cortical neuropil is dominated by unmyelinated substructures that
84 may significantly shape the diffusion MRI signal, possibly outweighing or otherwise complementing the
85 contribution of myelinated axons[29,30,31]. Further, it is known from previous work that myelin does not
86 necessarily drive the compartmentalization of water molecules underlying dMRI anisotropy, even in
87 myelinated axons, with lipid cell membranes being at least as important[31]. In the white matter, these
88 elements covary because the overwhelming majority of neurites are myelinated axons, so the
89 distinction between myelinated and unmyelinated neurites has not been of great importance[32].
90 However, given the greater tissue complexity of gray matter, recent theoretical and empirical studies
91 have begun to explicitly consider the contribution of unmyelinated tissue components[2,3,33].

92 The most conspicuous anatomical feature of the cerebral cortex is its laminar structure. Previous
93 dMRI studies investigating the cortex have consistently found that the principal diffusion direction is
94 perpendicular (henceforth, "vertical") to the pial surface, with the exception of thin zones directly
95 adjacent to the pial and white matter boundaries[3,34–36]. The diffusion orientations in white matter reflect
96 the organization of axonal projections into directed bundles. The predominance of vertical diffusion in
97 gray matter may reflect the organization of cell bodies, axons, dendrites and other tissue components
98 into columnar structures[2,3]. Vertically oriented tissue features in the gray matter include some
99 myelinated axons[22,23], but they also include, for example, apical dendrite bundles projecting vertically
100 from deep to superficial layers[3,33,37–39] as well as the neurites of many other more regional and layer
101 specific cell types[23,37,40].

102 In this study, we compared the spatial variation of dMRI anisotropy in the primate cerebral cortex
103 to a range of histological features revealed through common tissue stains. We performed high
104 resolution *ex vivo* MRI scans of the brain of a common marmoset (Callithrix jacchus) and subsequently
105 sectioned, stained, and co-registered the tissue, allowing for a pointwise comparison of dMRI fractional
106 anisotropy (dMRI-FA) and tissue features across the gray matter. We found that the spatial variation of
107 dMRI-FA showed little correspondence to that of myelin content, but that myelin content was instead
108 well captured by a different MRI measure, namely the magnetization transfer ratio (MTR). However, the
109 spatial variation of dMRI-FA corresponded well to that of structure tensor[41] derived histological

110 anisotropy (HA) computed from the same sections, and particularly to that produced from Nissl staining.
111 These findings bring to bear the important role of unmyelinated tissue components, such as the
112 prominent apical dendrites of infragranular pyramidal neurons[37–39], in shaping diffusion MRI signals in
113 the cortical gray matter.

114 Results

115 To assess the histological features underlying dMRI-FA in the primate cerebral cortex, we compared
116 *ex vivo* high-resolution dMRI data from the brain of a common marmoset, to histological sections
117 obtained from the same brain following the scanning session. The brain was scanned for 58 hours on a
118 7T Bruker preclinical scanner with 450mT/m gradient coils. Six whole-brain volumes at 150µm isotropic
119 resolution were averaged for each of 60 diffusion encoded directions and two B0 volumes. This
120 extensive averaging resulted in a dMRI dataset with a signal-to-noise ratio of approximately 85 in gray
121 matter. In addition, magnetization transfer ratio (MTR) volumes were acquired in a separate session
122 from the same brain at an isotropic spatial resolution of 75µm. The MTR sequence is known to be
123 sensitive to the myelin content of brain tissue[42]. The dMRI volumes were resampled to the higher MTR
124 resolution for analysis using a spline interpolation. After MRI scanning, the brain's left and right
125 hemispheres were sectioned into coronal and sagittal sections, respectively, at 50µm on a freezing
126 microtome. Adjacent sections were stained for Nissl bodies using the Thionin stain, and for myelin using
127 the Gallyas silver stain. For quantitative analysis, nine strips of gray matter in the dorsal frontal and
128 parietal lobes were chosen for comparison based on their low curvature, since cortical curvature can
129 affect observed dMRI-FA values[43]. Nonlinear registration was subsequently applied, allowing for a direct
130 and precise pixel to pixel comparison of diffusion and histological parameters at 150µm spatial scale
131 (see **Methods**, **SI Figure 1**).

132 *dMRI fractional anisotropy minimally reflects myelin content*

133 We began our analysis with a simple pixelwise correlation of MRI and histological stain intensity
134 within the nine registered sections. Our first question was whether the patterns of dMRI-FA matched
135 the distribution of myelin intensity, as might be expected based on some previous studies in white
136 matter regions[13,14]. We found that the spatial variation of dMRI-FA had poor correspondence to myelin
137 intensity both across laminae (henceforth, *vertically*) and along the cortical sheet (henceforth,
138 *horizontally*), as illustrated in a sagittal example section in **Figure 1a**. Comparing the dMRI-FA to the

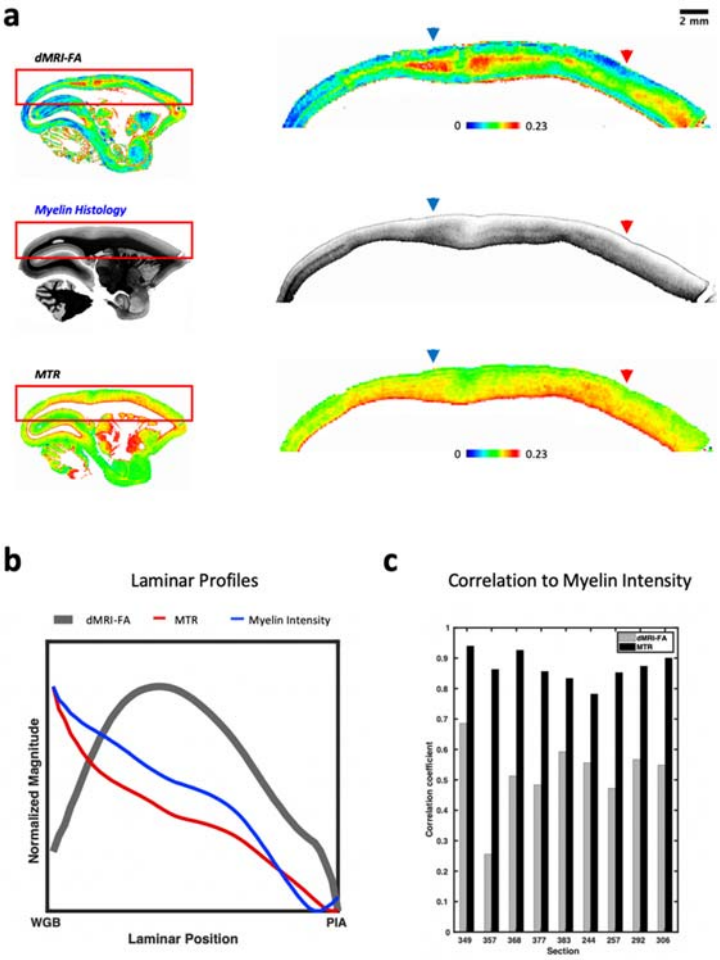

Figure 1. Comparison of dMRI FA to corresponding myelin histology and MTR MRI data obtained from the same tissue in the right hemisphere of marmoset monkey case P. ***a)*** *Sagittal sections of dMRI-FA (**top**), Myelin histology (**center**) and MTR MRI (**bottom**). The spatial variation of dMRI-FA in vertical (laminar) and horizontal direction showed minimal correspondence with the pattern of myelin intensity, but the variation of the MTR MRI closely mirrored the myelin variation. In some regions of high myelination, the dMRI-FA was high (red arrow) whereas in others it was low (blue arrow).* ***b)*** *Normalized average laminar profiles of FA, MTR and myelin intensity through the cortical thickness in the brain's left hemisphere, derived from cortical parcellation (see **Methods, Figure 3**).* ***c)*** *Histogram of correlation coefficients between MRI variables and histological myelin intensity over the nine sections of coronal histology used in this study. MTR MRI shows much higher correspondence with myelin intensity than dMRI-FA does.*

139 myelin stain intensity revealed areas of apparent matching (e.g. blue arrow) and others of clear
140 discrepancy (e.g. red arrow). In the vertical direction, myelin intensity declined monotonically from the
141 white matter to the pia[44]. This differed from the laminar pattern of dMRI-FA, which peaked in the
142 middle cortical layers (**Figure 1b**)[4,45]. In contrast to dMRI-FA, the MTR MRI contrast closely matched the
143 laminar pattern of myelin staining, as expected from the known sensitivity of the MTR MRI sequence to
144 large macromolecules[42]. The myelin intensity showed relatively poor correspondence to dMRI-FA
145 contrast and high correspondence to the MTR MRI contrast across all sections (**Figure 1c, SI Figure 2**).
146 We also found poor correspondence between dMRI-FA and Nissl stain intensity across all sections (**SI**
147 **Figure 2**).

148 *dMRI-FA reflects anisotropy of cortical tissue features*

149 Having established that myelin stain intensity was only modestly correlated to dMRI-FA, we next
150 turned our attention to histological features most directly related to anisotropy. We generated
151 parameter maps from the myelin and Nissl-stained sections based on the structure tensor (ST) model
152 (see **Methods**, **Figure 2, SI Figure 3**). Like the MRI-based diffusion tensor, the structure tensor derived
153 from histological images offers both vector and scalar information about the tissue, in the form of
154 principal orientations and ST coherence[46]. The ST calculation was weighted over a mesoscopic spatial
155 area that matched the dMRI acquisition resolution of 150μm (see **Methods**). Like the dMRI data, the
156 spatial variation of the ST parameters was resampled to 75μm for analysis. For both the myelin- and
157 Nissl-stained sections, the principal orientation of the ST was strikingly uniform and nearly always
158 perpendicular to the pial surface (i.e., vertical), corresponding well to the orientation map obtained
159 from the dMRI diffusion tensor (**Figure 2a**). While it was not the focus of the present study, we also
160 found that the 2D tractography computed from the histological ST and dMRI tensor data yielded
161 qualitatively nearly identical results (**SI Figure 4**). Only in thin laminar zones directly adjacent to the pia
162 and the white matter did this principal orientation deviate significantly from the vertical and differ
163 across measurements.

164

165

166 The histological ST coherence is similar to dMRI-FA in that it reflects the degree of alignment of
167 objects. However, unlike dMRI-FA[2,16], the magnitude of ST coherence does not incorporate the density
168 of oriented features within an area[46] (**SI Figure 3**). We therefore devised measures of histological
169 anisotropy (HA) that were more directly analogous to dMRI-FA by multiplying the histological ST
170 coherence values with a pixelwise approximation of neurite density. To derive HA from the myelin stain
171 (**myelin-HA**), we multiplied the myelin-based ST coherence with the normalized histological myelin
172 density. For Nissl data, we computed HA (**Nissl-HA**) as the product of Nissl ST coherence and the Nissl
173 derived "neurite fraction"[47] (see **Methods**). These measures served as summary statistics whose

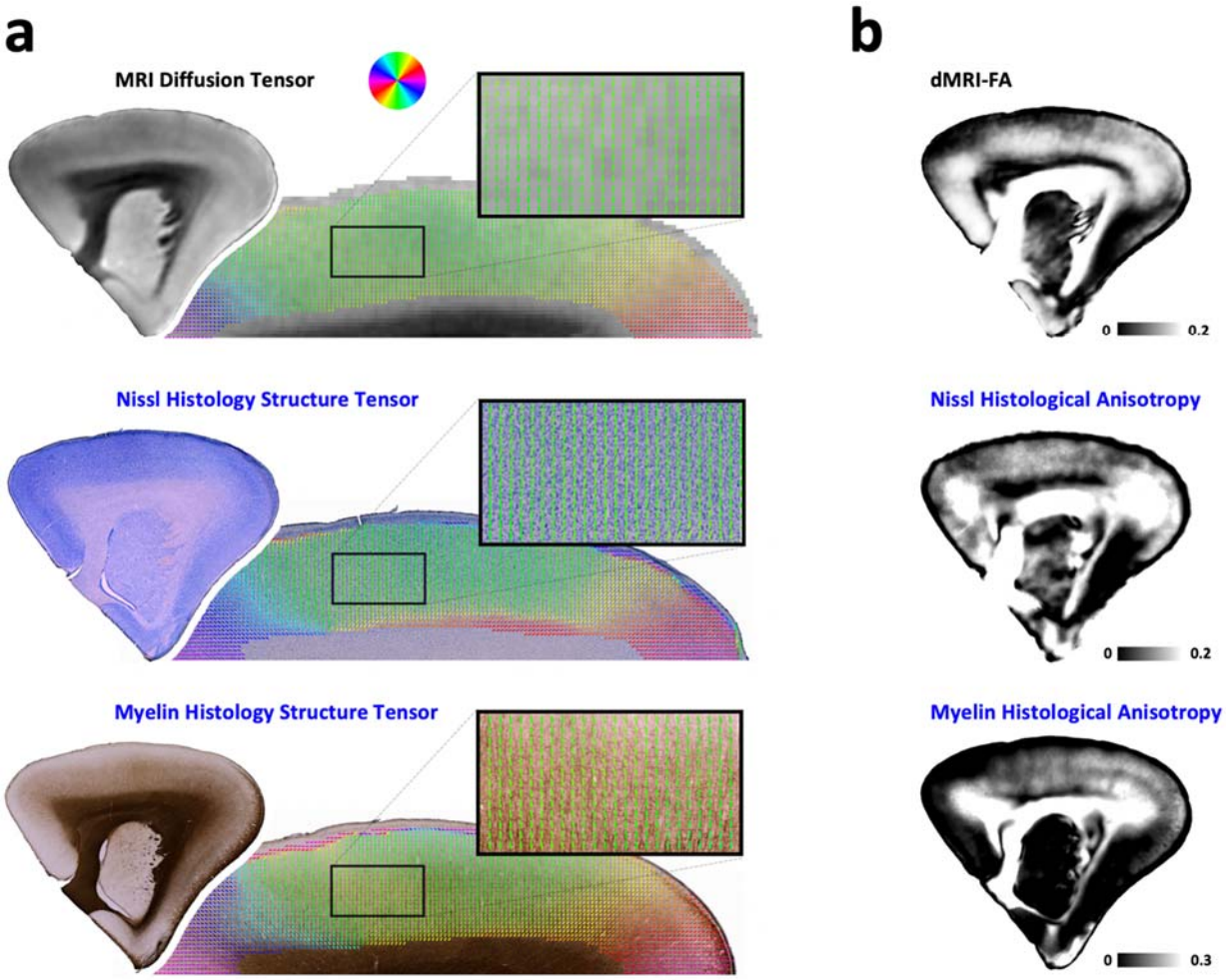

*Figure 2. Properties of directional MRI and histology data. For comparison with MRI data, the weighted structure tensor of the myelin and Nissl histology images was computed over a 150μm area (see **Methods**). **a**) Orientation data derived from Nissl and myelin histology and from dMRI are similar, showing columnar, vertically oriented vectors. The overall pattern of orientations in the gray matter is remarkably similar for the data computed from histology and from dMRI. **b**) The right column shows dMRI-FA and nonlinearly registered histology anisotropy maps which show the degree of edge dispersion from the mean in 75μm tiles (see **Methods**).*

variation could be compared systematically with that of the dMRI-FA across the gray matter (**Figure 2b**). While the inclusion of neurite density into the HA measure was deemed appropriate for this comparison, qualitatively similar results for all figures were obtained using maps of the histological coherence alone (**SI Figure 5**).

For each section, we quantitatively compared the spatial variation of dMRI-FA to the Nissl-HA, myelin-HA, and myelin stain intensity scalar parameter maps (see **Methods**). For completeness, we also compared the MTR MRI data to the same histological parameters. To accommodate anatomical variability and potential inconsistencies in histological stain intensity, we employed a parcellation approach in our analysis of the gray matter. In each of the nine low-curvature sections, we compared the spatial variation in the MRI and histological parameter maps by computing the correlation over multiple parcellated subdivisions spanning the thickness of the cortex (e.g. red trapezoids in **Fig. 3**, see **Methods, SI Figure 6**). We focused analysis on a horizontal parcellation width of 300µm along the pial boundary, though the results of the analysis were robust to parcel sizes ranging over a hundred-fold in

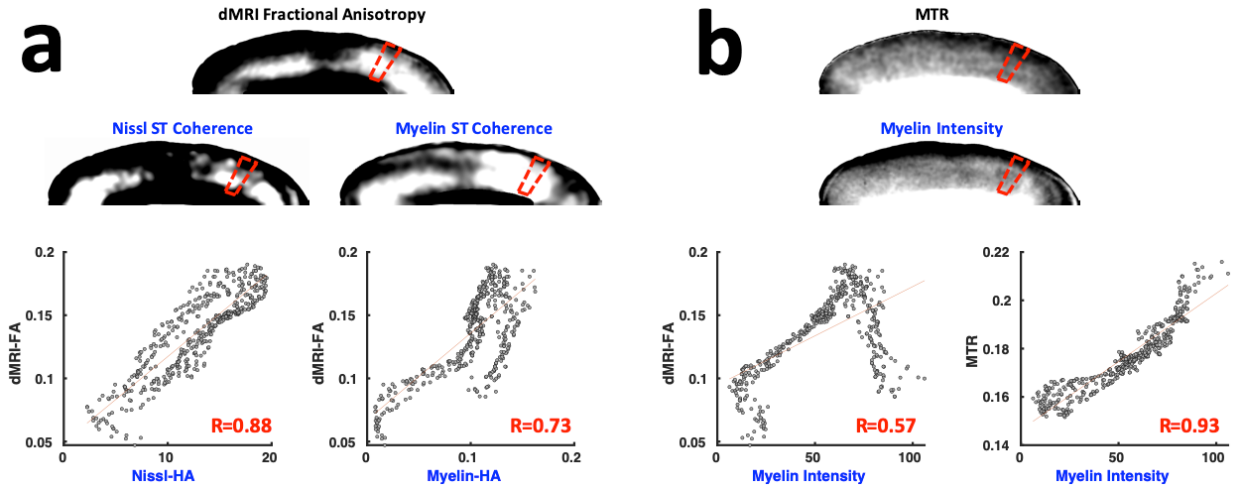

Figure 3.Example correlation of Histology and MRI variables sampled in columnar parcels. a) Comparison of dMRI fractional anisotropy to corresponding Nissl-HA and Myelin-HA from one parcel of corresponding tissue. b) Comparison of magnetic transfer ratio (MTR) MRI contrast with myelin intensity in same parcel as a). In both a) and b), the top row depicts nonlinearly co-registered histology parameter maps and MRI at 75µm resolution. The red trapezoids indicate a columnar parcel example. The bottom row shows representative pixelwise scatter plots of the co-registered data within the sample parcel of cortex, and Pearson correlation coefficients between histological variables and MRI variables.

area (see **SI Figure 7**). Within a given parcel, a pixel-by-pixel correlation of variation within each column revealed different levels of correspondence for the different histological and MRI parameters. This difference can be seen in the example parcel in **Figure 3**. For this parcel, the dMRI-FA showed the strongest spatial correspondence to the histological anisotropy of the Nissl-stained sections and

somewhat less to that of the myelin-stained section (**Figure 3a**, bottom). It did not correlate well with the profile of myelin intensity, which had a rather different laminar profile. However, the magnetization transfer ratio (MTR) MRI, exhibited a strong correlation with the myelin distribution (**Figure 3b**, bottom), consistent with previous findings[13,14].

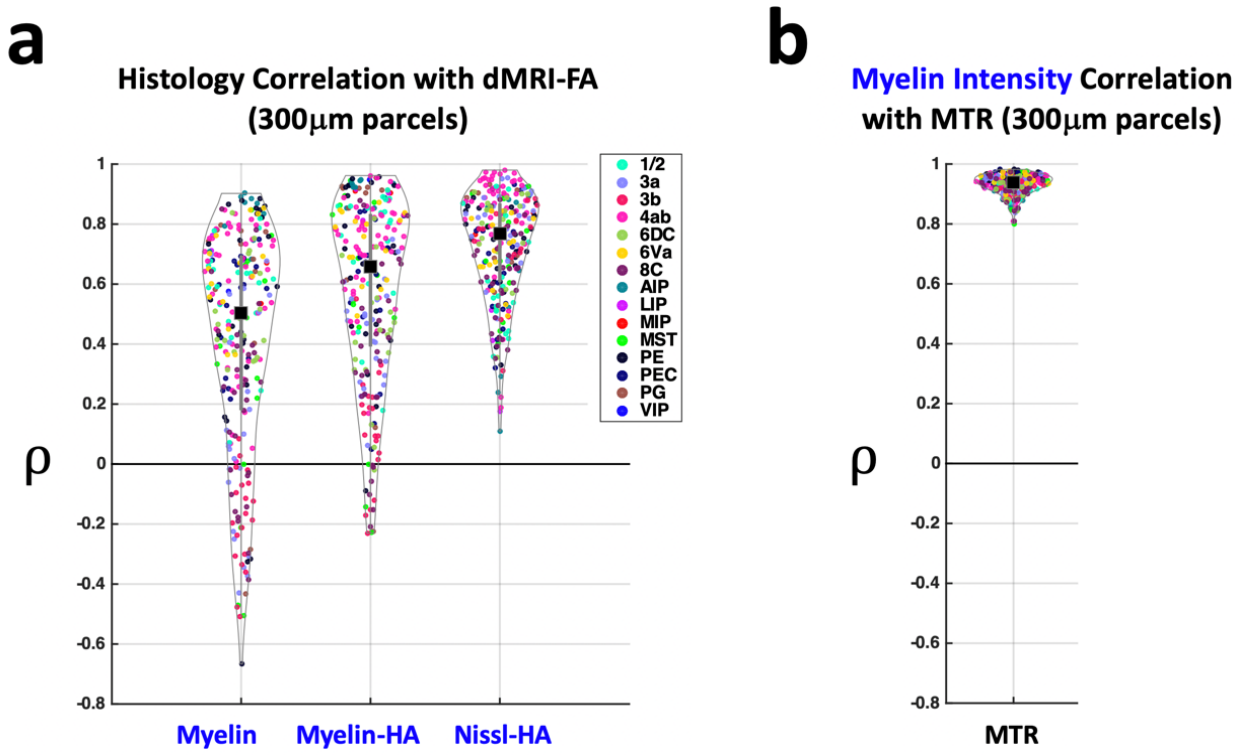

Figure 4 The distribution of correlation coefficients between histological parameters and dMRI-FA over all 393 parcels of cortex. ***a)*** *correlations of histology variables to dMRI-FA* ***b)*** *Correlation of MTR to Myelin Intensity. Each point in the distribution is the Pearson correlation between the variables sampled in a vertical parcel (see* ***Methods****). Colors indicate the anatomical region a parcel falls within. Black square shows median value and vertical gray bars show lower and upper quartiles. ρ indicates Pearson correlation coefficient.*

We evaluated such correlations across all 393 parcels in the nine sections for the different MRI and histological parameter maps, noting the anatomical region of each parcel with reference to the Paxinos et al atlas[48,49]. The distributions of dMRI-FA correlations across all parcels to the three histological parameter maps are shown in **Figure 4a**. The color of each point represents the cortical area from the atlas. Across the cortex, the Nissl histological anisotropy (Nissl-HA) showed consistently higher correlations with the dMRI-FA (ρ_{median} = 0.76, ρ_{mean} = 0.72) than did the myelin anisotropy (ρ_{median} = 0.63,

202 ρ_{mean} = 0.57) or myelin intensity (ρ_{median} = 0.47, ρ_{mean} = 0.39). The spatial maps of myelin intensity closely
203 matched those of the MTR MRI contrast (**Figure 4b)**, (ρ_{median} = 0.94, ρ_{mean} = 0.93). Nissl-HA and myelin-
204 HA were correlated moderately to one another (**SI Figure 7**). For all histological parameters, parcels with
205 relatively high and low tissue correlation coefficients were generally intermixed within each atlas area.
206 One exception to this intermixing was the correlation of dMRI-FA with agranular regions such as primary
207 motor cortex (4ab), which had notably high correlations. A similar pattern of results was obtained when
208 we substituted an in-plane, two-dimensional measure of dMRI anisotropy[41] for the three-dimensional
209 dMRI-FA measure (**SI Figure 8**). The closer correspondence of dMRI-FA to the Nissl- rather than the
210 myelin-stained tissue features indicates that, across the cerebral cortex, unmyelinated tissue structures
211 drive the spatial variation in high-resolution dMRI-FA maps.

212 Because fractional anisotropy can itself be broken down into diffusivity components, we further
213 investigated how each of these components tracked our measured tissue features. Fractional anisotropy
214 (dMRI-FA) is related to the ratio of axial diffusivity (AD) to radial diffusivity (RD), with the former
215 corresponding to diffusion along the principal diffusion axis, and the latter corresponding to diffusion
216 perpendicular to this axis. An increase in dMRI-FA can thus be effected either by a relative increase in
217 AD (vertical diffusivity) or a decrease in RD, and we found dMRI-FA was linked to both in the gray matter
218 (**SI Figure 9**). Previous work has established a strong association between lowered RD and myelin
219 content in coherently organized white matter[19], reflecting the tendency of myelin to restrict diffusion
220 perpendicular to axons. Consistent with these findings, we found that the spatial variation of RD was
221 strongly anticorrelated with that of both myelin stain intensity and myelin-HA in the cortical gray matter
222 (**SI Figure 9, SI Figure 10, SI Figure 11**). However, the spatial variation in axial diffusivity, quantifying
223 diffusion in the vertical direction, had no discernable relationship to myelin-HA, and was moderately
224 anticorrelated to myelin intensity. Nissl-HA was more modestly anticorrelated to RD, however unlike
225 myelin-HA it was also positively correlated to AD. These findings suggest that myelinated axons, though
226 tightly linked with the variation of RD, have only a secondary contribution to the overall spatial
227 distribution of dMRI anisotropy in the cerebral cortex.

228 *Horizontal variation in dMRI-FA is tracked by Nissl-HA, not myelin-HA*

229 Given that the laminar (vertical) and tangential (horizontal) dimensions of the cortex differ substantially
230 in their architectural variation, we performed additional analyses to consider these dimensions

separately. First, we addressed the vertical dimension. We analyzed the mean laminar variation of dMRI-FA and compared it to the histological anisotropy (**Figure 5a**). Collapsing the data across all horizontal cortical positions (see **Methods**) revealed a pronounced laminar profile for each of the measured parameters. The dMRI-FA profile had its highest responses in the middle or lower-middle cortical layers, with a decline in anisotropy in both upper layers, and lower layers near the white gray boundary (WGB). This profile was consistent with results from human dMRI[4], although our higher resolution data revealed significantly more underlying variation in the laminar profiles of individual horizontal locations (**SI Figure 12, SI Figure 13**). The average laminar profile of dMRI-FA across all horizontal regions in **Figure 5a** resembled the observed histological anisotropy, but with stronger correspondence to the Nissl-HA measure. In particular, like dMRI-FA, Nissl-HA took a low value near the white gray boundary and peaked in middle layers, but myelin-HA had a relatively high value in the deepest layers. As described earlier, the profile of dMRI-FA differed markedly from the more monotonic profiles of myelin intensity and MTR (**Figure 1c**). The average laminar Nissl-staining intensity exhibited nearly the inverse profile to the myelin intensity, having its highest intensity in the superficial layers (**SI Figure 14**).

246 Given these conspicuous average laminar profiles, we next asked whether the observed
247 correspondence between dMRI-FA and the two measures of histological anisotropy could be ascribed to
248 laminar variation alone, or also to variation in the horizontal direction, reflecting tissue differences
249 between anatomically defined cortical areas. To address this question, we shuffled the horizontal
250 locations of the columnar parcels in the histological parameter maps, relative to the locations of their
251 corresponding dMRI-FA parcels. If such shuffling were to have no effect on the observed parcel
252 correlations, then we could conclude that the results in **Figure 4** are fully explained by laminar variation
253 that follows a stereotypical pattern across the whole cortex.

254 We found that horizontal shuffling strongly affected the correlations of Nissl-HA with dMRI-FA, but
255 did not significantly change the myelin based histological/MRI correlations (**Figure 5b**). For Nissl-HA
256 only, horizontal shuffling caused the mean correlation to drop significantly, from 0.72 to 0.52 (t-test,
257 $p<10^{-10}$). These results indicate that the Nissl-HA measure has unique, region specific cytoarchitectural
258 correspondences to dMRI-FA that go beyond the laminar profile of the cortex in general. In contrast, the
259 relationships of myelin-HA and myelin intensity to dMRI-FA lack this regional specificity. In both those

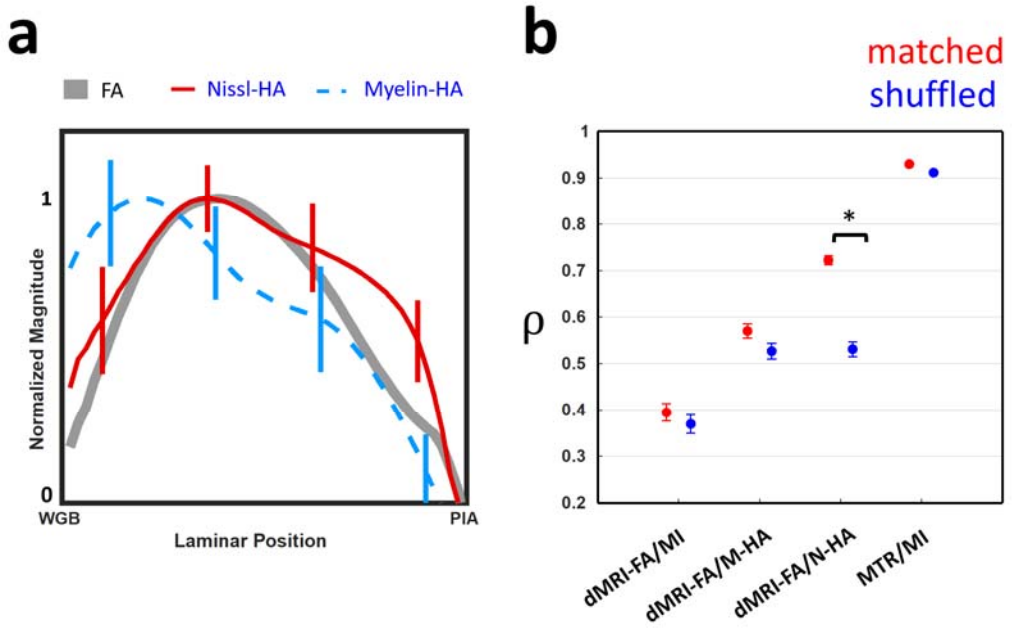

Figure 5 Average laminar profiles of FA, Nissl-HA and myelin-HA across all parcels, and the results of a spatial randomization condition to test the regional specificity of parcel-wise histology to MRI correlations. The results show Nissl-HA more closely matches the laminar profile of dMRI-FA, and is more sensitive to shuffling of horizontal MRI locations ***a)*** *Normalized laminar profiles of dMRI-FA, Myelin-HA and Nissl-HA through the cortical thickness, computed from the average of all columnar parcels (see* ***Methods****). WGB indicates the white/gray matter boundary, PIA indicates the pial surface (see* ***Methods, Figure 3****)* ***b)*** *The change in mean correlation coefficient when the cortical parcels of the histology parameters and those of the dMRI-FA are shuffled between random horizontal locations. Bars indicate standard error. The star indicates significance under a paired t-test. ρ indicates mean Pearson correlation coefficient*

260 cases, and in the case of the relationship between myelin intensity and MTR, the average laminar profile
261 in the cortex is sufficient to characterize the relationship between dMRI-FA and histology.

262 *Contribution of apical dendritic processes*

263 The peak value of dMRI-FA is in middle layers, approximately from layer 5 to layer 3, which is
264 congruent with Nissl-HA but differs from both myelin-HA and myelin density (see **Fig 5a**, **SI Figure 13**).
265 Nissl-HA serves as an indirect marker for unmyelinated tissue features. However, some evidence
266 suggests that it reflects, more than any other tissue component, the apical dendrites of layer 5
267 pyramidal neurons. These dendrites are exceptionally large-caliber unmyelinated neurites that run
268 vertically towards the pia, coalescing into bundles as they course through layer 4[22,37–39,50,51]. This
269 universal feature of isocortex has been described in detail in the macaque[38,39], human[52], rat[37,39,50], and
270 other species[39]. **Figure 6** shows an example of this prominent structural feature of the cerebral cortex in
271 a second marmoset subject, which we stained for the protein MAP-2 using immunohistochemical
272 methods. MAP-2 (microtubule associated protein) is a structural protein that is abundant in the soma
273 and dendrites of those pyramidal cells with the largest dendrites[38]. **Figure 6a** shows that the position

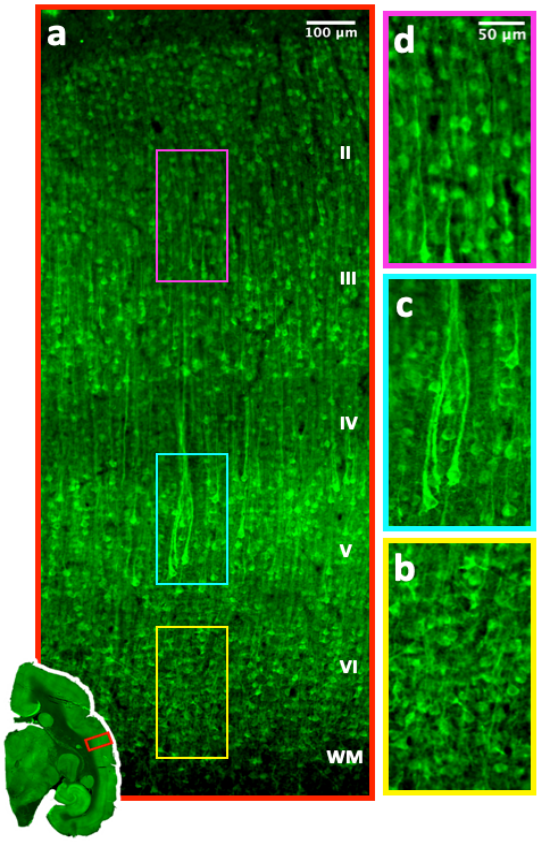

Figure 6 MAP-2 immunohostochemistry labelled tissue from a second marmoset qualitatively matches the profiles of dMRI-FA and Nissl-HA. ***a)*** *The stain reveals the larger apical dendrites and associated pyramidal cell bodies.* ***b)*** *In layer 6 cell body orientations and dendrites are smaller and incoherently organized* ***c)*** *Layer 5 pyramidal cell bodies are larger, orientated vertically and project large vertical dendrites which bundle as they proceed into layer 4* ***d)*** *Cell bodies in layers 3 and 2 are smaller and apical dendrites less visble*

and orientation of the pyramidal cell bodies reflect the orientation of their apical dendrites, and the overall vertical anatomy of cortex, with its bundles of large, unmyelinated dendrites[23,37–40].

The features revealed in the MAP-2 stained tissue (**Figure 6**) were consistent with both the principal diffusion orientation (**Figure 2**) and the peak diffusion anisotropy observed in the middle cortical layers (**Figure 5a**). In layer 6, the deepest, multiform cortical layer adjacent to the white matter, Nissl-HA and dMRI-FA take lower values than myelin-HA (**Figure 5a**). In this layer, pyramidal cell body orientations are reported in the literature as "tilted"[37,38] with dendrites emerging at a variety of angles. In **Figure 6b** we confirm this incoherence in the neurites of layer 6 in the marmoset (**Figure 6b**). It bears emphasis that this deepest portion of the cortex has the highest density of gray matter myelinated axons (**Figure**

283 **1a, Figure 1b**), and also high ST anisotropy of those axons, (**Figure 5a, SI Figure 13**) yet these do not lead
284 to elevated dMRI-FA in this location. In layer 5 and into layer 4 the MAP-2 labelled pyramids are larger,
285 more plentiful and more vertically oriented. Their dendrites tend to bundle together[37–39] as they project
286 upward (**Figure 6c**). Dendrites of infragranular pyramidal cells have their tufts in layer 4 or deep layer
287 3[37–39], thus forming a lower tier[37–39] of apical dendrite bundles. An upper tier of dendrites takes its origin
288 in the smaller, less coherently oriented pyramidal cells in Layers 2 and 3[37–39], reflected by the weaker
289 MAP-2 labelling in the marmoset (**Figure 6d**). Thus, while many tissue features may contribute to the
290 restriction of water diffusion in the circuitry of the cerebral cortex, the apical dendrites of layer 5
291 pyramidal neurons are a ubiquitous cortical feature that appear to have a particularly important role.

292

293 ## Discussion

294 The results of this study demonstrate that diffusion MRI in cortical gray matter can capture
295 important, hitherto inaccessible cytoarchitectural tissue properties in vivo. We compared histological
296 data to fractional anisotropy of the diffusion tensor (dMRI-FA), a widely used and straightforward dMRI
297 parameter with minimal *a priori* assumptions about tissue properties[53]. Our point-by-point analysis
298 (**Figure 3**, **Figure 4**) of exceptionally high resolution, finely co-registered dMRI-FA and histological
299 parameter maps from the same brain indicated that, in contrast to many findings in the white
300 matter[13,14], myelin does not principally shape the mesoscale variation of diffusion anisotropy in the
301 cerebral cortex .

302 On deeper investigation, we found that myelin density and histological anisotropy tended to
303 take high values in the deepest cortical layers, while both dMRI-FA and Nissl histological anisotropy took
304 high values in the central cortical layers (**Figure 1b, Figure 5a**). Importantly, we found that the pattern of
305 dMRI-FA correlations with Nissl-HA was disrupted by shuffling the horizontal locations of the tissue
306 parcels, but the correlations with myelin-based parameters were not (**Figure 5b**). This suggests dMRI-FA
307 is predominantly shaped by the regional cytoarchitectonic differences reflected in Nissl-HA, rather than
308 by the myeloarchitecture. We found that these results are consistent with patterns found in apical
309 dendrites, notably the vertically projecting, bundled apical dendrites of layer 5 neurons [23,37–40,50–52,54].
310 This is a universal feature of the cerebral cortex, and these dendrites may be strong contributors to the
311 restriction of diffusion (**Figure 6**).

312 The cerebral cortex is characterized by distinct anatomical zones, or regions, and the properties
313 of these regions may be tracked by dMRI-FA. However, many distinct cortical maps have been proposed,
314 based on different cytoarchitectural, myeloarchitectural, connectional and functional properties[55,56]. Our
315 cortical parcellation strategy (**Methods**, **Figure 3**, **SI Figure 6**) was designed to accommodate this variety,
316 by systematically assessing the tissue over many differently sized subdivisions (**SI Figure 7**). Our results
317 were robust to a range of parcel sizes, whose horizontal extents spanned two orders of magnitude. This
318 tolerance to parcel size suggests the correlation results were minimally affected by changes in stain
319 properties within a section, or by parcels that spanned cytoarchitectural boundaries. Similarly, the
320 absence of an obvious correspondence between the observed parcel correlations, and any particular
321 cytoarchitectonic regions, indicates that the high point-by-point correlations between Nissl-HA and
322 dMRI-FA we observed are a feature that generalizes over the cortex.

323 An exception to this general pattern was found in layer 4 of granular cortex, where there was
324 sometimes a mismatch between low Nissl-HA, and high dMRI-FA (**SI Figure 15a**), leading to somewhat
325 diminished correlations. The relatively lower Nissl-HA values in layer 4 likely stemmed from the
326 predominance of round granular cell bodies. Given the vertical orientation in cortex, the high dMRI-FA
327 values[4,5] in layer 4 most likely reflect the prominence of apical dendrite bundles coursing through the
328 granular layer toward the pial surface[23,37–40,50–52,54], an organization that was strongly evident in our
329 MAP-2 staining. Other neurites, such as layer IV terminals of thalamic afferent axons[57] (**SI Figure 15b**),
330 and the unmyelinated, vertical axons of layer 4 cells themselves[23], likely contribute to the restricted
331 diffusion in this layer as well. In areas of relatively low granularity, these apical dendrites are adequately
332 indicated by orientation cues in the Nissl stain. However, in highly granular areas, the Nissl-HA indicates
333 diminished anisotropy in layer 4.

334 The specific association of Nissl-HA and dMRI-FA outside of layer 4 is likely related to the
335 arrangement of the cell bodies into cellular minicolumns for which apical dendrite bundles are thought
336 to provide a substructure[23,37–40,52,54]. Cellular minicolumns in Nissl stained data have been used to detect
337 and quantify the architecture of the cortex[23,58–60], and recent studies have begun to explore their
338 relationships to parameters derived from the diffusion tensor in ex-vivo human data[61,62]. Apical dendrite
339 bundles exhibit a hexagonal packing structure when viewed in tangentially sectioned tissue[37,52,54]. In the
340 vertical plane, soma of all cell types are packed vertically along the cells of this honeycomb-like
341 structure[37,52,54], and these packed cell bodies exhibit composite vertical edges[52], which are likely to be

342 detected by our structure tensor methods[23,37,38,40,63] (**SI Figure 2**). A similar structure tensor based
343 method has very recently been applied to detect white matter fiber bundle orientations via
344 arrangements of oligodendrocytes in Nissl data[64].

345 In addition to apical dendrites, dMRI-FA is likely also shaped by other unmyelinated tissue features,
346 such as the axons of double bouquet cells[23,39] or layer IV terminals of thalamic afferent axons[57].
347 Immunohistochemical stains for proteins such as MAP τ[65], SMI-312[66], SMI-311[66], GFAP[67] and others may
348 be useful to investigate the relative contributions of other non-myelinated tissue features, though
349 quantification of neurite structure is difficult using antibody staining. For example, MAP-2 is a protein
350 implicated in microtubule assembly, which is disproportionately expressed in the largest dendrites, thus
351 leaving thinner dendrites unstained, even if they are numerous[37]. The specific combination of tissue
352 features that shape cortical dMRI-FA cannot be fully known at this point and may well differ between
353 anatomical regions. Further research is required to understand the columnar anatomy of the cortex
354 itself[37,63], especially in a quantitative way. With that said, the strong spatial covariation (median 0.76) of
355 Nissl-HA to dMRI-FA, and the regional specificity of that relationship, holds promise that the structural
356 basis of diffusion MRI in the cortex can be well understood.

357 Our finding that Nissl-HA and myelin-HA correlated in distinct ways to the diffusivity components of
358 dMRI-FA may offer some further clues to its anatomical basis. We found that the cortical variation of
359 dMRI-FA, which is related to the ratio of axial to radial diffusivity, was as strongly driven by increases in
360 its axial component as by decreases in its radial one (**SI Figure 9**). In the samples of gray matter we
361 studied, AD is always diffusivity in the vertical direction, perpendicular to the pial surface. Of the
362 histological measures, only Nissl-HA positively correlated with axial diffusivity. Myelin-HA did not have a
363 consistent relationship to AD, however it did have a notably strong and negative relationship to radial
364 diffusivity (**SI Figure 9b, SI Figure 11**), indicating its known role in restricting diffusion perpendicular to
365 the orientation of axons[19,20]. However, the strong anti-correlation of RD and myelin-HA did not predict
366 the spatial variation of dMRI-FA per se, which was strongly driven by variation in axial diffusivity. We do
367 not yet know why Nissl-HA and dMRI-FA reliably covary with AD, while myelin parameters and MTR do
368 not. However, unlike myelinated axons, apical dendrites have a reliably vertical orientation[23,37–40,52,54].
369 Combined with their large numbers, and potentially also with differences in intrinsic diffusivity between
370 neurites[68], variations in apical dendrite density may be responsible for this effect.

371 The distinct diffusivity profiles of myelin-HA and Nissl-HA are a matter for further research, because
372 they might be used in biophysically motivated models of the diffusion signal[12,68,69] that can distinguish
373 between myelinated and non-myelinated tissue compartments. In dMRI models of white matter, it is
374 sometimes assumed that the intrinsic rate of diffusion in the axoplasm parallel to the membrane is
375 constant[68,70]. In the more heterogenous environment of gray matter, this assumption may not hold[12]
376 and instead, the cytoplasm of different cell compartments may have distinct intrinsic diffusivities[31].
377 Recent modelling efforts in white matter have sought to simultaneously measure variation in intra-
378 axonal diffusivity, and variation in axon orientation[68]. Related biophysical models may prove especially
379 important in gray matter. Models that include myelin levels, cortical curvature[61,62] and location in the
380 cortical depth may be able to gather very detailed information about the human cortex in-vivo.

381 Accurate gray matter diffusion models for applications related to human health must be
382 grounded in decisive empirical data. The variation of diffusion MRI parameters may reflect valuable
383 information such as cytoarchitectural differences between cortical regions, or degradation of tissue due
384 to disease[61,62]. Measurements taken in-vivo at low resolution will represent the influences not only of
385 cyto and myeloarchitecture, but also of cortical curvature[43,61,62]. High resolution data in ex-vivo animal
386 models is important for establishing the histological basis of signals that can be obtained in humans,
387 now or in the near future as imaging capacities continue to improve. In our exceptionally high resolution
388 ex-vivo dMRI data, we found the cortex was dominated by structures running perpendicular to the pial
389 surface, and the simple diffusion tensor model was sufficient to capture the variation in anisotropy.
390 However, when imaging the brain at lower resolution in-vivo, more complex models may be necessary
391 to represent the heterogeneous tissue properties contained within the much larger voxels. The
392 marmoset brain has a cortical thickness and cytoarchitectural complexity that is similar to the human,
393 and it can be used as a model of human neurodegenerative processes[71]. Moreover, its small brain
394 volume and lissencephalic cortex allows for the study histological dMRI correlates in detail and at high
395 resolution, without the effects of curvature. This information may form a basis for the interpretation of
396 signals from the highly gyrencephalic human brain scanned at lower resolution[61,62].

397 Diseases such as Alzheimer's are believed to involve subtle changes to tissue properties
398 especially in their early stages, and the ability to gather specific cytoarchitectural information separately
399 from myeloarchitectural in-vivo may be crucial[10], particularly since relatively little post-mortem
400 information is available regarding the early tissue changes. The early stages of Alzheimer's and other

401 diseases of the gray matter neuropil can manifest as cellular damage and inflammation rather than
402 demyelination[72]. Changes in mean diffusivity in gray matter have been associated with Alzheimer's
403 pathology[73]. The present findings may inform the development of dMRI models of the gray matter,
404 perhaps to specifically target neuroinflammation[10] or other aspects of Alzheimer's pathology in the
405 earliest stages.

406 Methods

407 We describe below the methods used in this study, sample preparation and MRI acquisition,
408 sectioning and staining, registration and finally statistical analysis.

409 *Animals and materials*

410 The brain of one adult marmoset (female, 5-year-old, "Case P") from a previous study[48] was used for MRI
411 to histology comparison. Tissue from a second brain, (female, 2-year-old, "Case F"), was obtained from an
412 unrelated study to examine the MAP2 immunohistochemistry.

413 *Ex vivo high-resolution MRI Acquisition*

414 Before MRI scanning, the formalin-fixed marmoset brain of case P was soaked with 0.15%
415 gadopentetate dimeglumine (Magnevist, Bayer Leverkusen, Germany) for 3 weeks to reduce the T1
416 relaxation time. In order to improve SNR, brain P was cut through the midline, and each hemisphere was
417 scanned separately with a 25-mm birdcage volume coil.

418 For the left hemisphere Diffusion MRI was collected with a 3D diffusion-weighted spin-echo EPI
419 sequence with a spatial resolution of 150µm isotropic voxel size. The 3D diffusion EPI sequence
420 parameters were: TR = 400 ms, TE = 28.4 ms, flip angle = 90°, FOV = 38.4 x 24 x 21 mm, matrix size = 256
421 x 160 x 140, resolution = 0.15 mm isotropic. Sixty two DWI volumes (2 at b=0, and 60 directions with
422 b=4800) were acquired using 3 averages. The same 62 volumes were collected a second time with
423 identical settings. The total DWI acquisition time was about 58 hours. The pulse width for the diffusion
424 weighting gradient is 6.4 ms and pulse separation is 14 ms.

425 The right hemisphere was scanned with 100µm resolution. The parameters for the 3D diffusion-
426 weighted spin-echo EPI sequence were: TR = 400 ms, TE = 35 ms, flip angle = 90°, FOV = 38.4 x 20 x 25

427 mm, matrix size = 348 x 200 x 250, resolution = 0.10 mm isotropic, a total of 132 DWI images (6 at b=0,
428 and 126 directions with b = 4800), and total acquisition time was about 55 hours.

429 The left and right hemispheres separately underwent scanning for MTR at 75µm and 150µm
430 respectively.

431 The MTR images were collected with a 3D FLASH sequence. For the resolution of 150µm, the
432 parameters were: TR = 21.5 ms, TE = 3.6 ms, flip angle = 20^0, FOV = 38.4 x 24 x 21 mm, matrix size = 256
433 x 160 x 140, number of averages = 8 and number of repetitions = 6, total acquisition time about 13 hour
434 For the resolution of 75µm acquisition, the parameters are: TR = 21.9 ms, TE = 3.8 ms, flip angle = 20^0,
435 FOV = 34.8 x 20.4 x 20.1 mm, matrix size = 464 x 272 x 268, number of averages=5 and number of
436 repetition = 14, total acquisition time about 60 hours. The magnetization transfer was achieved (in M_{sat}
437 scans) by a Gaussian shaped pulse at +2000 Hz offset frequency in one scan and at -2000 Hz in the other
438 scan of a paired acquisition; the duration of pulse is 12.5 ms and flip angle is 540^0 and the pulse is
439 present in every TR. This magnetization transfer pulse is turned off in M_{off} scans. The MTR value is
440 calculated as $100*(1-M_{sat}/M_{off})$.

441 *MRI Processing*

442 *Diffusion Tensor Estimation* dMRI data was preprocessed using TORTOISE v3[74] which includes code
443 for denoising[75]. After rotation to the histology slice plane (see *Registration of histology and MRI data*
444 below), the diffusion tensor was estimated using FSL 5.0.11 DTIFIT. AD, RD and the in-plane anisotropy[41]
445 were calculated using FSL 5.0.11 fslmaths.

446 For estimation of cytoarchitectural boundaries, we registered the Paxinos et al atlas[48] to the left
447 hemisphere of case P MTR using ANTS[76]

448 Registered dMRI tensor parameter maps and MT data were split into separate coronal 32 bit
449 quantitative tif images and grouped according to slice number for registration.

450

451 *Histological Processing of MRI brain*

452 Case P's left hemisphere was coronally sectioned at 50µm on a freezing microtome, while the right
453 hemisphere was sectioned sagittally. Alternate sections were stained for Nissl bodies and for myelin.
454 The Gallyas silver stain for myelin was selected to stain individual axons in high detail[77]. We used the
455 Thionin stain for Nissl bodies. This is a traditional staining method that identifies cell bodies and some
456 dendrites proximal to the soma, but very few axons[78]. Each histological section was scanned at 0.88µm
457 resolution (10x magnification) using a Zeiss Axioscan microscope slide scanner. Higher resolution
458 0.44µm microscopy produced similar ST results. Nine matched pairs of Thionin/Gallyas stained sections
459 were selected for non-linear registration based on criteria of even staining and minimal damage.

460 *MAP-2 Immunohistochemistry*

461 The brain of a second marmoset, case F, was used to gather MAP-2 immunohistochemistry. The brain's
462 right hemisphere was sectioned at 40 µm on a freezing microtome. A free-floating brain section was
463 submitted to the heat-induced epitope retrieval to enhance immunolabeling by incubating it for 30
464 minutes in 10 mM Tris-EDTA buffer (pH 9.5) at 80°C[79]. Then the section was incubated for 60 h at 4°C
465 with a 1:200 dilution of a rabbit anti MAP-2 primary antibody (188 003, Synaptic Systems, Germany) and
466 for 3 h with a 1:250 dilution of a goat anti-rabbit secondary antibody conjugated to DyLight 680
467 fluorophore (35569, Invitrogen, Waltham, Ma). Finally, the section was mounted on a glass slide, air-
468 dried, and cover-slipped with DEPEX mounting media (13515, Electron Microscopy Sciences, Hatfield,
469 PA). What is the scan resolution?

470 *Registration of histology and MRI data*

471 *Rigid body rotation to histology slice plane.* For histology to MRI registration, we first performed an
472 initial rigid body alignment of the 75µm M_{sat} data (**SI Figure 1**) to match the histology slice plane for each
473 of P's hemispheres. This transformation was estimated by-eye using the mango MRI editor/viewer[80] and
474 the manually transformed MT volume was used as the target for FSL 5.0.11 FLIRT[81] to transform the
475 remainder of the MRI data.

Registration of MT and dMRI. The 150µm dMRI was rigid body registered to the 75µm MT volume using FSL FLIRT, and in doing so the dMRI was upsampled to 75µm using spline interpolation. The b-vectors were rotated using the FAST transform and custom MATLAB code.

MIND nonlinear registration of local histology ROI. After performing ST computations on the histology to produce ST anisotropy parameter maps (see *Structure Tensor Analysis of Histological Orientations and Anisotropy* below), we performed careful nonlinear alignment of nine local frontal and parietal ROI from the histology to the MRI (**SI figure 1**). 75µm resolution stain intensity maps of nine coronal sections of each of Nissl and myelin histology were first binarized using a threshold adjustment in imageJ[82] and then registered to their corresponding MRI slices to correct for histology shrinkage and deformation, first using manual 2D alignment in imageJ[82] and then MIND MATLAB code[83] (α=0.1). To avoid registration between MRI and histological features whose anatomical meanings and relationships were unknown, the registration source and target images were featureless gray matter masks gray matter derived from the MT data (**SI figure 1**). Custom MATLAB code was written to store and apply these transforms to ST maps (see *Structure Tensor Analysis of Histological Orientations and Anisotropy* below) and other parameter maps derived from the histology. We selected regions of frontal and parietal cortex for nonlinear alignment whose minimal gyrification ensured that the diffusion MRI signal was largely unaffected by cortical curvature[43]. This registration process allowed us to directly compare the cortical variation of diffusion and histological parameters from the same brain.

Structure Tensor Analysis of Histological Orientations and Anisotropy

To estimate the anisotropy and orientation content of the histology we employed the structure tensor method[41]. The 0.88µm per pixel resolution histology images were processed using the structure tensor as implemented in the "OrientationJ" ImageJ package[46], using a local gaussian window of σ=80 pixels and image gradients computed with a cubic spline. This was applied to the color channel of the histology that exhibited the strongest image intensity gradients. This was the red channel for Nissl data, or blue channel for Gallyas myelin data. Orientation and anisotropy information were obtained from these data according to

$$S_0[p] = \begin{bmatrix} I_x[p]I_x[p] & I_x[p]I_y[p] \\ I_x[p]I_y[p] & I_y[p]I_y[p] \end{bmatrix}$$

Equation 1*. Pixelwise structure tensor*

where S_0 is the structure tensor at pixel p and Ix, Iy are the partial derivatives of the 2D image intensities at pixel p. Since the dMRI data contains diffusion information gathered over a 150µm cubic area, the histology structure tensor at each pixel was a distance weighted function S_w[p] of the structure tensors S_0 within a radius of 75µm. This was achieved for pixel p by multiplying with gaussian window with a sum of 1, with sigma 85 pixels (75µm), shown in **Equation 2.** The ST angle is shown in **Equation 3** and anisotropy in **Equation 4** and **SI Figure 15**

$$S_w[p] = \sum_r w[r] S_0[p-r]$$

Equation 2. *Weighted structure tensor*

$$\theta[p] = \frac{1}{2} arctan\left(2\frac{I_x[p]I_y[p]}{I_y[p]I_y[p] - I_x[p]I_x[p]}\right)$$

Equation 3. *ST orientation*

$$SCoherence = \frac{\lambda_1 - \lambda_2}{\lambda_1 + \lambda_2}$$

Equation 4. *Structure tensor coherence (λ indicate eigenvalues of the structure tensor)*

A pipeline was implemented in bash and ImageJ macro language to process the Zeiss axioscan histology output files in CZI format into 32 bit tif format with resolution 0.88µm, and process these with orientationJ. The histology stain intensity data and ST data at 0.88µm were then down sampled into maps of 75µm tiles for comparison and registration to MRI data using MATLAB R2018a. The mean ST angle within 75µm was the circular mean of the 0.88µm angles within that area. Because ST anisotropy is sensitive to coherence of image edges, we verified that individual myelinated axons were visible on our 50 · m sections in the deepest, most myelin heavy layers of the GM (**SI Figure 16**). We also verified that ST coherence maps were equivalent at different focal depths in the tissue (**SI Figure 17**).

Histological Anisotropy Because diffusion anisotropy is sensitive to both the density and coherence of tissue features, but ST coherence is sensitive only to the latter, we defined composite measures of

529 histological anisotropy. Myelin-HA was defined as the product of myelin stain intensity and the ST
530 coherence of the myelin data.

531 For the Nissl-HA we defined the neurite fraction (NF) as 1-Nissl intensity, where the highest gray
532 matter value was mapped to 1 and black was mapped to 0. Nissl-HA was defined as the product of NF
533 and the ST coherence of the Nissl data.

534 *2D dMRI and Histology ST Tractography*

535 The ST analysis of the myelin and Nissl histology yielded 2D vector fields at 75μm resolution
536 representing the mean 0.88μm ST angle within a tile. For comparison, we projected the 3D dMRI
537 principal eigenvector at the same spatial resolution onto the 2D plane (**Figure 2**).
538
539 The vector fields of the 75μm weighted structure tensor permitted tractography based on histological
540 image properties within areas equivalent to the MRI voxels. We ran identical tractography through the
541 Nissl and myelin ST vector fields. We used a MATLAB package "even streamlines" v 1.1.0.0 to ensure the
542 streamlines were evenly spaced in the horizontal direction[84], modified to use a fixed integration step of
543 0.1 . **SI Figure 4** shows tractography through the 2D projected components of the first eigenvector of the
544 diffusion tensor, overlaid on high resolution histology images. We note all three modalities yield very
545 similar results.

546 *Cortical Parcellation and Statistical Analysis*

547 To sample the gray matter for analysis, we took advantage of the fact that cortex consists of vertically
548 oriented tissue components[22,34,37,85] to develop a matrix representation whose columns were derived
549 from data sampled along the vertical dMRI tractography streamlines (**SI Figure 6a**) (see *2D dMRI and*
550 *Histology ST Tractography* above), and whose rows spanned the horizontal direction. We first masked
551 the registered gray matter ROI by thresholding the MT image (M_{sat}), and eroding this mask by 2 75μm
552 pixels to avoid the regions where the diffusion tensor orientations were known not to be vertical (see
553 **Figure 2**). We then ran tractography through the 2d projected principal **SI Figure 6** eigenvectors of the
554 diffusion tensor in the masked region. This produced a set of vertical, non-intersecting streamlines (**SI**
555 **Figure 6a)** which were numbered from in the horizontal direction.

556 For each histology and MRI parameter map, we sampled a vector of unique pixels whose coordinates
557 intersected one streamline's coordinates. We then resampled each resulting vector of pixels to a fixed
558 length using bilinear interpolation, to yield a simple matrix representation of the gray matter (**SI Figure**
559 **6a**). This operation was invertible such that data in matrix form could be displayed in image space (**SI**
560 **Figure 6b**).

561 Our statistical analysis proceeded by parcellating the matrix representation of the nonlinearly registered
562 histology and MRI data. We used parcellation in our analysis partly to separate out regions of potentially
563 differing stain intensity, and partly because different anatomical regions of cortex have different
564 constituent myelo- and cytoarchitectural elements[22,38] and may therefore exhibit different relationships
565 between histology and dMRI. For each parcel we took the Pearson correlation between sample
566 variables. Examples are shown in **Figure 3**. **SI Figure 6b** shows parcels of matrix columns of different
567 sizes, represented in image space and colored by the correlation coefficient of histology ST anisotropy to
568 dMRI-FA.

569 **Figure 4** and **Figure 6** show the distribution of correlation coefficients using a parcel size of 5 streamlines
570 which is roughly 300µm in horizontal width. **SI Figure 6** shows that the correlation results are stable for
571 different parcel sizes. For **figure 5** we concatenated matrices from all sections and displayed the mean of
572 all rows. **SI figure 9** shows the mean of rows in each individual section.

573

574

575 ## *References*

576 1. Aggarwal, M., Nauen, D. W., Troncoso, J. C. & Mori, S. Probing region-specific microstructure of
577 human cortical areas using high angular and spatial resolution diffusion MRI. *Neuroimage* **105**,
578 198–207 (2015).

579 2. Assaf, Y. Imaging laminar structures in the gray matter with diffusion MRI. *Neuroimage* **197**, 677–
580 688 (2019).

581 3. Leuze, C. W. U. *et al.* Layer-specific intracortical connectivity revealed with diffusion MRI. *Cereb.*
582 *Cortex* **24**, 328–339 (2014).

583 4. Truong, T.-K., Guidon, A. & Song, A. W. Cortical Depth Dependence of the Diffusion Anisotropy in
584 the Human Cortical Gray Matter In Vivo. *PLoS One* **9**, e91424 (2014).

585 5. Kleinnijenhuis, M. *et al.* Layer-specific diffusion weighted imaging in human primary visual cortex
586 in vitro. *Cortex* **49**, 2569–2582 (2013).

587 6. Jespersen, S. N., Leigland, L. A., Cornea, A. & Kroenke, C. D. Determination of Axonal and Dendritic
588 Orientation Distributions Within the Developing Cerebral Cortex by Diffusion Tensor Imaging. *IEEE*
589 *Trans. Med. Imaging* **31**, 16–32 (2012).

590 7. Jespersen, S. N. *et al.* Neurite density from magnetic resonance diffusion measurements at
591 ultrahigh field: Comparison with light microscopy and electron microscopy. *Neuroimage* **49**, 205–
592 216 (2010).

593 8. Seehaus, A. *et al.* Histological validation of high-resolution DTI in human post mortem tissue. *Front.*
594 *Neuroanat.* **9**, 1–12 (2015).

595 9. Brodmann, K. *Vergleichende lokalisationslehre der großhirnrinde in ihren prinzipien dargestellt auf*
596 *grund des zellenbaues (1909)(English translation available in Garey, L.J. (2006). Brodmann's:*
597 *Localisation in the cerebral cortex. 3rd Edition. Springer US)*. (Springer US, 2006).

598 10. Weston, P. S. J., Simpson, I. J. A., Ryan, N. S., Ourselin, S. & Fox, N. C. Diffusion imaging changes in
599 grey matter in Alzheimer's disease: A potential marker of early neurodegeneration. *Alzheimer's*
600 *Res. Ther.* **7**, 1–8 (2015).

601 11. O'Doherty, D. C. M., Chitty, K. M., Saddiqui, S., Bennett, M. R. & Lagopoulos, J. A systematic review
602 and meta-analysis of magnetic resonance imaging measurement of structural volumes in
603 posttraumatic stress disorder. *Psychiatry Res. - Neuroimaging* **232**, 1–33 (2015).

604 12. Lampinen, B. *et al.* Searching for the neurite density with diffusion MRI: Challenges for biophysical
605 modeling. *Hum. Brain Mapp.* **40**, 2529–2545 (2019).

606 13. Mancini, M. *et al.* An interactive meta-analysis of MRI biomarkers of Myelin. *Elife* **9**, 1–23 (2020).

607 14. Lazari, A. & Lipp, I. Can MRI measure myelin? Systematic review, qualitative assessment, and meta-
608 analysis of studies validating microstructural imaging with myelin histology. *Neuroimage* **230**,
609 117744 (2021).

610 15. Calamante, F., Jeurissen, B., Smith, R. E., Tournier, J. D. & Connelly, A. The role of whole-brain
611 diffusion MRI as a tool for studying human in vivo cortical segregation based on a measure of
612 neurite density. *Magn. Reson. Med.* **79**, 2738–2744 (2018).

613 16. Fukutomi, H. *et al.* Neurite imaging reveals microstructural variations in human cerebral cortical
614 gray matter. *Neuroimage* **182**, 1–12 (2018).

615 17. Roosendaal, S. D. *et al.* Regional DTI differences in multiple sclerosis patients. *Neuroimage* **44**,
616 1397–1403 (2009).

617 18. Song, S. K. *et al.* Diffusion tensor imaging detects and differentiates axon and myelin degeneration
618 in mouse optic nerve after retinal ischemia. *Neuroimage* **20**, 1714–1722 (2003).

619 19. Song, S. K. *et al.* Dysmyelination revealed through MRI as increased radial (but unchanged axial)
620 diffusion of water. *Neuroimage* **17**, 1429–1436 (2002).

621 20. Song, S. K. *et al.* Demyelination increases radial diffusivity in corpus callosum of mouse brain.
622 *Neuroimage* **26**, 132–140 (2005).

623 21. Stricker, N. H. *et al.* Decreased white matter integrity in late-myelinating fiber pathways in

Alzheimer's disease supports retrogenesis. *Neuroimage* **45**, 10–16 (2009).

22. Peters, A. & Sethares, C. Myelinated axons and the pyramidal cell modules in monkey primary visual cortex. *J. Comp. Neurol.* **365**, 232–255 (1996).

23. Buxhoeveden, D. P. & Casanova, M. F. The minicolumn hypothesis in neuroscience. *Brain* **125**, 935–951 (2002).

24. Lewis, J. W. & Van Essen, D. C. Mapping of architectonic subdivisions in the macaque monkey, with emphasis on parieto-occipital cortex. *J. Comp. Neurol.* **428**, 79–111 (2000).

25. Van der Weijden, C. W. J. *et al.* Myelin quantification with MRI: A systematic review of accuracy and reproducibility. *Neuroimage* **226**, 117561 (2020).

26. Glasser, M. F. & Van Essen, D. C. Mapping human cortical areas in vivo based on myelin content as revealed by T1- and T2-weighted MRI. *J. Neurosci.* **31**, 11597–11616 (2011).

27. Kleinnijenhuis, M. *et al.* Detailed laminar characteristics of the human neocortex revealed by NODDI and histology. *Organ. Hum. Brain Mapp.* 3815 (2013).

28. Vogt, C. & Vogt, O. Allgemeinere Ergebnisse unserer Hirnforschung. *J Psychol Neurol* **25**, 279–461 (1919).

29. Schüz, A., Braitenberg, V. & Miller, S. R. The Human Cortical White Matter: Quantitative Aspects of Cortico-Cortical Long-Range Connectivity. in *Cortical Areas* 377–385 (CRC Press, 2002).

30. Wang, Y., Ye, M., Kuang, X., Li, Y. & Hu, S. A simplified morphological classification scheme for pyramidal cells in six layers of primary somatosensory cortex of juvenile rats. *IBRO Reports* **5**, 74–90 (2018).

31. Beaulieu, C. The basis of anisotropic water diffusion in the nervous system - A technical review. *NMR Biomed.* **15**, 435–455 (2002).

32. Jones, D. K., Knösche, T. R. & Turner, R. White matter integrity, fiber count, and other fallacies: The do's and don'ts of diffusion MRI. *Neuroimage* **73**, 239–254 (2013).

33. Jespersen, S. N., Kroenke, C. D., Østergaard, L., Ackerman, J. J. H. & Yablonskiy, D. A. Modeling dendrite density from magnetic resonance diffusion measurements. *Neuroimage* **34**, 1473–1486 (2007).

34. Reveley, C. *et al.* Superficial white matter fiber systems impede detection of long-range cortical connections in diffusion MR tractography. *Proc. Natl. Acad. Sci.* **112**, E2820–E2828 (2015).

35. Miller, K. L. *et al.* Diffusion imaging of whole, post-mortem human brains on a clinical MRI scanner. *Neuroimage* **57**, 167–181 (2011).

36. McNab, J. A. *et al.* High resolution diffusion-weighted imaging in fixed human brain using diffusion-weighted steady state free precession. *Neuroimage* **46**, 775–785 (2009).

37. Rockland, K. S. & Ichinohe, N. Some thoughts on cortical minicolumns. *Exp. Brain Res.* **158**, 265–277 (2004).

38. Peters, A., Manuel Cifuentes, J. & Sethares, C. The organization of pyramidal cells in area 18 of the rhesus monkey. *Cereb. Cortex* **7**, 405–421 (1997).

39. Peters, A. The Morphology of Minicolumns. *Neurochem. Basis Autism From Mol. to Minicolumns*

662 1–295 (2010) doi:10.1007/978-1-4419-1272-5.

663 40. Buxhoeveden, D. P. & Casanova, M. F. The minicolumn and evolution of the brain. *Brain. Behav.*
664 *Evol.* **60**, 125–151 (2002).

665 41. Budde, M. D. & Frank, J. A. Examining brain microstructure using structure tensor analysis of
666 histological sections. *Neuroimage* **63**, 1–10 (2012).

667 42. Heath, F., Hurley, S. A., Johansen-Berg, H. & Sampaio-Baptista, C. Advances in noninvasive myelin
668 imaging. *Dev. Neurobiol.* **78**, 136–151 (2018).

669 43. Kleinnijenhuis, M. *et al.* Diffusion tensor characteristics of gyrencephaly using high resolution
670 diffusion MRI in vivo at 7T. *Neuroimage* **109**, 378–387 (2015).

671 44. Bock, N. A., Hashim, E., Kocharyan, A. & Silva, A. C. Visualizing myeloarchitecture with magnetic
672 resonance imaging in primates. *Ann. N. Y. Acad. Sci.* **1225**, E171–E181 (2011).

673 45. Liu, C. *et al.* Marmoset Brain Mapping V3: Population multi-modal standard volumetric and
674 surface-based templates. *Neuroimage* **226**, 117620 (2021).

675 46. Püspöki, Z., Storath, M., Sage, D. & Unser, M. Transforms and operators for directional bioimage
676 analysis: A survey. *Adv. Anat. Embryol. Cell Biol.* **219**, 69–93 (2016).

677 47. Spocter, M. A. *et al.* Neuropil distribution in the cerebral cortex differs between humans and
678 chimpanzees. *J. Comp. Neurol.* **520**, 2917–2929 (2012).

679 48. Liu, C. *et al.* A digital 3D atlas of the marmoset brain based on multi-modal MRI. *Neuroimage* **169**,
680 106–116 (2018).

681 49. Paxinos, G., Watson, C., Petrides, M., Rosa, M. & Tokuno, H. The Marmoset Brain in Stereotaxic
682 Coordinates. (2013).

683 50. Peters, A. & Walsh, T. M. A study of the organization of apical dendrites in the somatic sensory
684 cortex of the rat. *J. Comp. Neurol.* **144**, 253–268 (1972).

685 51. Peters, A. & Kara, D. A. The neuronal composition of area 17 of rat visual cortex. IV. The
686 organization of pyramidal cells. *J. Comp. Neurol.* **260**, 573–590 (1987).

687 52. Gabbott, P. L. A. Radial organisation of neurons and dendrites in human cortical areas 25, 32, and
688 32'. *Brain Res.* **992**, 298–304 (2003).

689 53. Basser, P. J., Mattiello, J. & LeBihan, D. MR diffusion tensor spectroscopy and imaging. *Biophys. J.*
690 **66**, 259–267 (1994).

691 54. Gabbott, P. & Bacon, S. . The organisation of dendritic bundles in the prelimbic cortex (area 32) of
692 the rat. *Brain Res.* **730**, 75–86 (1996).

693 55. Stephan, K. E. & Kotter, R. One cortex - many maps: An introduction to coordinate-independent
694 mapping by Objective Relational Transformation (ORT). *Neurocomputing* **26–27**, 1049–1054
695 (1999).

696 56. Passingham, R. E., Stephan, K. E. & Kotter, R. The anatomical basis of functional localization in the
697 cortex. *Nat. Rev. Neurosci.* **3**, 606–616 (2002).

698 57. Oberlaender, M. *et al.* Cell type-specific three-dimensional structure of thalamocortical circuits in
699 a column of rat vibrissal cortex. *Cereb. Cortex* **22**, 2375–2391 (2012).

58. Chance, S. A. *et al.* Microanatomical correlates of cognitive ability and decline: Normal ageing, MCI, and Alzheimer's disease. *Cereb. Cortex* **21**, 1870–1878 (2011).

59. Cruz, L. *et al.* Age-related reduction in microcolumnar structure in area 46 of the rhesus monkey correlates with behavioral decline. *Proc. Natl. Acad. Sci. U. S. A.* **101**, 15846–15851 (2004).

60. Buldyrev, S. V. *et al.* Description of microcolumnar ensembles in association cortex and their disruption in Alzheimer and Lewy body dementias. *Proc. Natl. Acad. Sci. U. S. A.* **97**, 5039–5043 (2000).

61. McKavanagh, R. *et al.* Relating diffusion tensor imaging measurements to microstructural quantities in the cerebral cortex in multiple sclerosis. *Hum. Brain Mapp.* **40**, 4417–4431 (2019).

62. Torso, M., Bozzali, M., Zamboni, G., Jenkinson, M. & Chance, S. A. Detection of Alzheimer's Disease using cortical diffusion tensor imaging. *Hum. Brain Mapp.* **42**, 967–977 (2021).

63. Jones, E. G. Microcolumns in the cerebral cortex. *Proc. Natl. Acad. Sci. U. S. A.* **97**, 5019–5021 (2000).

64. Schurr, R. & Mezer, A. A. The glial framework reveals white-matter fiber architecture in human and primate brains. **7960**, 1–11 (2021).

65. Kosik, K. S., Joachim, C. L. & Selkoe, D. J. Microtubule-associated protein tau (τ) is a major antigenic component of paired helical filaments in Alzheimer disease. *Proc. Natl. Acad. Sci. U. S. A.* **83**, 4044–4048 (1986).

66. Ulfig, N., Nickel, J. & Bohl, J. Monoclonal antibodies SMI 311 and SMI 312 as tools to investigate the maturation of nerve cells and axonal patterns in human fetal brain. *Cell Tissue Res.* **291**, 433–443 (1998).

67. Eng, L. F. & Ghirnikar, R. S. GFAP and Astrogliosis. *Brain Pathol.* **4**, 229–237 (1994).

68. Howard, A. F. D. *et al.* Estimating intra-axonal axial diffusivity with diffusion MRI in the presence of fibre orientation dispersion. *bioRxiv* 1–33 (2020).

69. Novikov, D. S., Fieremans, E., Jespersen, S. N. & Kiselev, V. G. Quantifying brain microstructure with diffusion MRI: Theory and parameter estimation. *NMR Biomed.* **32**, 1–53 (2019).

70. Zhang, H., Schneider, T., Wheeler-Kingshott, C. A. & Alexander, D. C. NODDI: Practical in vivo neurite orientation dispersion and density imaging of the human brain. *Neuroimage* **61**, 1000–1016 (2012).

71. Sato, K. *et al.* A non-human primate model of familial Alzheimer's disease. *bioRxiv* 2020.08.24.264259 (2020).

72. Wenk, G. L. Neuropathologic changes in Alzheimer's disease. *J. Clin. Psychiatry* **64**, 7–10 (2003).

73. Montal, V. *et al.* Cortical microstructural changes along the Alzheimer's disease continuum. *Alzheimer's Dement.* **14**, 340–351 (2018).

74. Irfanoglu, M. O., Nayak, A., Jenkins, J. & Pierpaoli, C. TORTOISE v3 : Improvements and New Features of the NIH Diffusion MRI Processing Pipeline. in *ISMRM 25th annual meeting* 9–11 (2018).

75. Veraart, J. *et al.* Denoising of diffusion MRI using random matrix theory. *Neuroimage* **142**, 394–406 (2016).

76. Avants, B. B. *et al.* A reproducible evaluation of ANTs similarity metric performance in brain image registration. *Neuroimage* **54**, 2033–2044 (2011).

77. Gallyas, F. Silver staining of myelin by means of physical development. *Neurol. Res.* **1**, 203–209 (1979).

78. Windle, W. F., Rhines, R. & Rankin, J. A Nissl Method Using Buffered Solutions of Thionin. *Stain Technol.* **18**, 77–86 (1943).

79. Jiao, Y. *et al.* A simple and sensitive antigen retrieval method for free-floating and slide-mounted tissue sections. *J. Neurosci. Methods* **93**, 149–162 (1999).

80. Lancaster, J. L. *et al.* Automated regional behavioral analysis for human brain images. *Front. Neuroinform.* **6**, 1–12 (2012).

81. Jenkinson, M., Bannister, P., Brady, M. & Smith, S. Improved Optimization for the Robust and Accurate Linear Registration and Motion Correction of Brain Images. *Neuroimage* **17**, 825–841 (2002).

82. Schindelin, J. *et al.* Fiji: An open-source platform for biological-image analysis. *Nat. Methods* **9**, 676–682 (2012).

83. Heinrich, M. P. *et al.* MIND: Modality independent neighbourhood descriptor for multi-modal deformable registration. *Med. Image Anal.* **16**, 1423–1435 (2012).

84. Jobard, B. & Lefer, W. Creating Evenly-Spaced Streamlines of Arbitrary Density. in *Proceedings of the Eurographics Workshop in Boulogne-sur-Mer France* 43–55 (1997).

85. Pierpaoli, C., Jezzard, P., Basser, P. J., Barnett, A. & Di Chiro, G. Diffusion tensor MR imaging of the human brain. *Radiology* **201**, 637–648 (1996).

Acknowledgements

This research was supported by the Intramural Research Program of the National Institute of Mental Health (ZIC MH002899 to DAL and ZIA MH002951 to YC). C.R. and R.B.M. were supported by the Wellcome Centre for Integrative Neuroimaging (Wellcome Trust, 203139/Z/16/Z), and a Biotechnology and Biological Sciences Research Council grant to RBM (BBSRC UK,BB/N019814/1). High resolution MRI data was collected on the 7T Bruker scanner of Dr. Afonso Silva in NINDS. Scanning of brain sections was carried out in the Systems Neuroscience Imaging Resource under Dr. Ted Usdin in NIMH. The authors thank David Yu for histology processing.

768 ## Author contributions

769 C.R. Devised and initiated the study; C.R., F.Q.Y, R.B.M and D.A.L. designed research; F.Q.Y. acquired
770 data; C.R. analysed data; D.A.L. and F.Q.Y. refined the analysis strategy; D.M. conducted the MAP-2
771 immunohistochemistry; C.R. wrote the initial manuscript draft; D.A.L., F.Q.Y., D.M., Y.C. and R.B.M.
772 edited the manuscript; All authors discussed results.

773 ## Competing Interests

774 The authors declare no competing interests.

775